Supporting Information for

Ultrafast Electron Microscopy of Nanoscale Charge Dynamics in Semiconductors

Michael Yannai[1], Raphael Dahan[1], Alexey Gorlach[1], Yuval Adiv[1], Kangpeng Wang[1], Ivan Madan[2], Simone Gargiulo[2], Francesco Barantani[2,3], Eduardo J. C. Dias[4], Giovanni Maria Vanacore[5], Nicholas Rivera[6], Fabrizio Carbone[2], F. Javier García de Abajo[4,7], Ido Kaminer[1]*

[1]Technion - Israel Institute of Technology; Haifa 3200003, Israel.
[2]Institute of Physics, École Polytechnique Fédérale de Lausanne; Station 6, Lausanne, 1015, Switzerland.
[3]Department of Quantum Matter Physics, University of Geneva; 24 Quai Ernest-Ansermet, 1211, Geneva 4, Switzerland.
[4]ICFO-Institut de Ciencies Fotoniques, The Barcelona Institute of Science and Technology, 08860 Castelldefels (Barcelona), Spain.
[5]Department of Materials Science, University of Milano-Bicocca; Via Cozzi 55, 20121, Milano, Italy.
[6]Massachusetts Institute of Technology; Cambridge MA 02139, USA.
[7]ICREA-Institució Catalana de Recerca i Estudis Avançats; Passeig Lluís Companys 23, 08010 Barcelona, Spain.

*Corresponding author. Email: kaminer@technion.ac.il

This PDF file includes:

Supplementary Text
Figures S1 to S3
Captions for Movies S1 to S3

Other Supporting Information for this manuscript include the following:

Movies S1 to S3

Supplementary Text

Theory of charge dynamics electron microscopy (CDEM)

In this section, we introduce a theoretical description of charge-dynamics electron microscopy (CDEM). First, we present a theory of the interaction of swift electrons with arbitrary classical electromagnetic fields described by a general set of potentials (scalar and vector potentials). We show how CDEM may be described by the same theoretical apparatus which has been successfully applied to describe the interactions of swift electrons with strong optical fields, as used in photon-induced near-field electron microscopy (PINEM).[45–47,49] The framework discussed in this section generalizes prior treatments to cases in which the fields are described by both a vector and a scalar potential. Prior work has operated in a gauge in which the scalar potential is eliminated; this is always possible, but in many cases (especially in near-field optics), an approximate description in terms of a pure scalar potential (*via* Coulomb's law) can prove convenient. Additionally, certain gauges necessarily include a scalar potential, such as the Lorenz gauge, for which a straightforward calculation connects the source terms and the potentials. We employ a general unspecific-gauge approach to derive a master equation for the electron wave function after interacting with the fields created by the studied charge dynamics in the specimen (*e.g.*, such as an irradiated semiconductor producing THz near fields *via* the photo-Dember effect, as described in the main text for our experiment).

We show how this master equation, taken in its classical limit, describes quite accurately the observed energy losses in the CDEM experiments presented in the main text. The classical limit of this theory is sufficient when the electron pulse duration is substantially shorter than a single field cycle, so the electron can be treated as a point particle, as is approximately the case in our experiment. Using the fact that the experiments are well-described by the classical limit of this theory, we then develop a second, complementary theory of CDEM which is purely classical (making no reference to electron wave functions). We shall refer to this second theory as the "classical theory of CDEM". In the classical approach, the observed energy loss is modeled by calculating the work done on a classical point charge (the electron) by the electric force associated with the fields created by the charge dynamics.

1. Review of quantum theory of swift electron interactions with classical EM fields

In this section, we adopt a quantum-mechanical formalism to describe the interaction of the probe electron with an effective potential $\Pi(\mathbf{r}, \mathrm{t})$ that contains both the vector and scalar potentials. This unified quantum theory can be understood as a generalization of the theory of PINEM[46,47] to the case of a wide-bandwidth field,[51] such as the THz field in our experiment. The unified theory also describes the regimes of so-called anomalous-PINEM.[55] Importantly, all assumptions regarding the free electron used in previous works (*e.g.*, PINEM) on swift-electron interactions with EM fields (*e.g.*, electron paraxiality) are retained here, and are generally applicable in transmission electron microscopy setups.[46,47] We assume a relativistic free-electron pulse with a narrow energy distribution centered around $U_0 = \sqrt{m^2c^4 + \hbar^2c^2k_0^2}$ and narrow momentum distribution centered around $\boldsymbol{p}_0 = \hbar k_0 \hat{\boldsymbol{z}}$ (associated with an "unperturbed" rectilinear velocity v). Further assuming that the interaction energy with the electromagnetic field is far smaller than the electron energy $U_0 = \gamma mc^2$ (norecoil approximation), we may formulate a simple Hamiltonian description of the particle in terms of the effective potential Π.

To do so, we start from the approximate Hamiltonian for an energetic relativistic particle in an external electromagnetic field:[78]

$$H_R \approx U_0 + \frac{c^2(-i\hbar\nabla + e\boldsymbol{A})^2 + m^2c^4 - (U_0 + e\Phi)^2}{2(U_0 + e\Phi)}$$
$$\approx U_0 + \frac{c^2(-i\hbar\nabla + e\boldsymbol{A})^2 + m^2c^4 - (U_0 + e\Phi)^2}{2\gamma mc^2}, \quad \text{(S1)}$$

where we have used $e\Phi \ll U_0$. Expanding the squares and ignoring quadratic terms in Φ and $\boldsymbol{A}$ (as well as identity terms) we obtain

$$H_R = \frac{-\hbar^2\nabla^2 - 2ie\hbar\boldsymbol{A}\cdot\nabla + m^2c^2 - \frac{U_0^2}{c^2} - \frac{2U_0e\Phi}{c^2}}{2\gamma m}. \quad \text{(S2)}$$

Defining the electron wave function in terms of its envelope as $\psi = \phi e^{ik_0z - iU_0t/\hbar}$, one finds

$$i\hbar\partial_t\phi = H\phi, \quad \text{(S3)}$$

with $H = -i\hbar\boldsymbol{v}\cdot\nabla + e\boldsymbol{v}\cdot\boldsymbol{A} - e\Phi \equiv -i\hbar\boldsymbol{v}\cdot\nabla + \Pi$, and where

$$\Pi(\boldsymbol{r}, t) = e\boldsymbol{v}\cdot\boldsymbol{A} - e\Phi. \quad \text{(S4)}$$

In deriving this result, we have neglected $\nabla\cdot\boldsymbol{A}$ (arising from the relation $\nabla\cdot\boldsymbol{A}/k_0\boldsymbol{A} \ll 1$). Taking the electron wave function to be of the form $\psi(z,t) \equiv \phi(z,t)e^{ik_0z - iU_0t/\hbar}$, with $\phi(z,t)$ denoting the envelope wave function, and considering $|k_0\phi| \gg |\nabla\phi| = |\partial_z\phi|$ (paraxial approximation), the Schrödinger equation may simply be written as

$$(\partial_t + v\partial_z)\phi(z,t) = \frac{1}{i\hbar}\Pi(z,t)\phi(z,t). \quad \text{(S5)}$$

To find this expression, we have expanded the square root in powers of $\nabla\phi$ and retained only terms up to the first derivative. Making the standard change of variables $z' = z - vt, t' = t$, Eq. (S5) may be written as

$$\partial_{t'}\phi = \frac{1}{i\hbar}\Pi(z' + vt', t')\phi, \quad \text{(S6)}$$

admitting the solution $\phi(z',t') = \phi_0(z')\exp\left[-\frac{i}{\hbar}\int_{-\infty}^{t'} ds\ \Pi(z' + vs\,, s)\right]$. Expressed in terms of z, t, this solution can be recast into

$$\phi(z,t) = \phi_0(z - vt)\exp\left[-\frac{i}{\hbar}\int_{-\infty}^{t} ds\ \Pi(z + vs - vt, s)\right]. \quad \text{(S7)}$$

It is important to note that this expression is consistent with previous treatments for which the scalar potential vanishes and then the expression above reduces to (using Eq. (S4) for Π)

$$\phi(z,t) = \phi_0(z - vt)\exp\left[-\frac{iev}{\hbar}\int_{-\infty}^{t} ds\ A_z(z + vs - vt, s)\right]. \quad \text{(S8)}$$

This expression is identical to that in references 43 and 46. In the CDEM experiment described in the main text, A_z is equal to zero (see the following section on the hydrodynamic model), and thus we can replace Π by the scalar potential $-e\Phi$ (using Eq. (S4)).

Simulation of the measured EELS data (*i.e.*, electron spectrum versus time-delay) is carried out by first evaluating the Fourier transform of the electron coherent wave function with respect to time at the detector plane, where a time-delay variable Δt is introduced in the incident electron wave function $\phi_0\big(z - v\cdot(t + \Delta t)\big)$, representing the varying pump-probe time-delay in our experiment. The squared modulus of this wave function is then convoluted in energy-shift ($\Delta\mathcal{E}$) and time-delay space with an incoherent broadening function – a two-dimensional chirped Gaussian of the form $\exp(-a\Delta t^2 - 2b\Delta t\Delta\mathcal{E} - c\Delta\mathcal{E}^2)$. The chirp b is added here to accommodate for the electron pulse

dispersion, resulting from the electron emission process and free-space propagation inside the TEM column. The chirp parameter can be obtained experimentally, through fitting the above chirped Gaussian to one of the energy side-bands obtained in a PINEM-type experiment.[35]

2. Classical limit of the general formalism

Here, we work out a classical limit for the electron wave function after interaction with an arbitrary field, starting from the quantum-mechanical formalism reviewed above and assuming that the fields vary negligibly over the duration of the electron pulse. In this section, we choose a gauge with no scalar potential, allowing us to use Eq. (S8).

The classical limit is associated with the fact that, in the present work, the electron wavepacket duration is shorter than the THz field cycle. In this situation, the electron essentially behaves as a classical point charge. It is then pertinent to Taylor-expand the slowly varying vector potential $A_z(z-vt+z',t')$ around small values of $z-vt$, assuming the centroid of the electron wavepacket to follow the trajectory $z=vt$. Thus, the argument of the exponential in Eq. (S8) can be expressed as (for the post-interaction electron at $t\to\infty$):

$$-\frac{ie}{\hbar}\int_{-\infty}^{\infty} v\,dt'\left(A_{\mathrm{z}}(vt',t')+\partial_{z'}A_{\mathrm{z}}(z',t')|_{z'=vt'}(z-vt)+O((z-vt)^2)\right). \qquad \text{(S9)}$$

The term independent of $z-vt$ in this expansion contributes an overall phase $\varphi=-(ev/\hbar)\int_{-\infty}^{\infty}dt'\,A_z(vt',t')$ that does not affect the transmitted electron spectrum (i.e., its energy distribution). Using the relation $\partial_t A(vt,t)=v\partial_{z'}A(z',t')|_{z'=vt';\,t'=t}+\partial_{t'}A(z',t')|_{z'=vt';\,t'=t}$, the term linear in $z-vt$ can be expressed as $i/\hbar\int_{-\infty}^{\infty}v\,dt'\,(-eE_z(vt',t'))\cdot(z/v-t)$. Here, we have used $E=-\partial_t A$ and noted that, for a finite-duration field, the boundary term associated with the integral of $\partial_{t'}A$ vanishes. The integral over t' simply represents the work done on the charge by the electric field, assuming the trajectory $z=vt$, as mentioned above. To see this, we recall that the work done by a conservative force $\boldsymbol{F}(\boldsymbol{r},t)$ on a particle moving along a trajectory $\boldsymbol{r}(t)$ is simply given by $\Delta\mathcal{E}=\int dt\,\boldsymbol{F}(\boldsymbol{r}(t),t)\cdot\boldsymbol{v}(t)$. Therefore, the envelope wave function of the post-interaction electron can be written in the form

$$\phi(z,t)=\phi_0(z,t)e^{i\varphi}\exp[i(\Delta\mathcal{E}/\hbar)(z/v-t)]. \qquad \text{(S10)}$$

In summary, the wave function in Eq. (S10) is the incident one multiplied by an irrelevant phase factor $e^{i\varphi}$ as well as by a plane wave $\exp[i(\Delta\mathcal{E}/\hbar)(z/v-t)]$ representing a rigid energy shift by $\Delta\mathcal{E}$ (and a corresponding change in momentum by $\Delta\mathcal{E}/v$ within the nonrecoil approximation). Corrections of higher-order terms in the aforementioned Taylor expansion may become relevant for electron wavepacket durations similar to or larger than the field cycle.

3. Fully classical description of energy loss of swift electrons

Given that the electron energy spectrum observed in CDEM can be understood using the classical work done by the fields on a point charge, it is of interest to develop a conceptually simpler and purely classical theory of CDEM. The classical theory amounts to (1) calculating the EM fields that act on the impinging electrons (this step is shared with the quantum theory), (2) calculating the classical work done on the electron, and (3) averaging over the initial electron distribution to get the statistics of energy loss that is experimentally probed. For the latter, the distribution refers to the electron pulse duration, which determines a variance in the electron arrival time, as well as the electron energy width, which broadens the measured energy spectrum.

In order to evaluate the electron energy shift in the classical limit, one must first find the electric and magnetic fields resulting from the above potentials:

$$\boldsymbol{E} = -\nabla\Phi - \frac{\partial \boldsymbol{A}}{\partial t}, \quad \boldsymbol{B} = \nabla \times \mathbf{A}. \tag{S11}$$

We next calculate the Lorentz force generated by the fields:

$$\boldsymbol{F} = -e(\boldsymbol{E} + v \times \mathbf{B}). \tag{S12}$$

Defining the electron trajectory along z as

$$s(t) = z_0 + v(t - \Delta t), \tag{S13}$$

the mean electron energy shift is then given by:

$$\Delta\mathcal{E}(\Delta t) = \int_{t_\mathrm{i}}^{t_\mathrm{f}} F \cdot v dt = \int_{s_\mathrm{i}}^{s_\mathrm{f}} F_z ds\,, \tag{S14}$$

where in the rightmost expression, the paraxiality assumption has been applied, implying that the electron velocity is directed exclusively along z. Moreover, under the quasi-static approximation, the magnetic field term in the Lorentz force can be neglected. For instance, in our experiment, this approximation is justified because the electron distance from the crystal is considerably smaller than the THz wavelength ($x_\mathrm{electron} \cong 10\ \mu\mathrm{m} \ll \lambda_\mathrm{THz} \cong 600\ \mu\mathrm{m}$). Therefore, we are left with

$$F_z = -eE_z, \quad E_z = -\frac{\partial\Phi}{\partial z} - \frac{\partial A_z}{\partial t}. \tag{S15}$$

In the final step of the calculation, the mean electron energy shift $\Delta\mathcal{E}(\Delta t)$ is represented in energy-shift and time-delay space using a sum of delta functions:

$$\Delta\mathcal{E}(\Delta t, \mathcal{E}) = \sum_{\Delta t_i} \delta\big(\Delta t - \Delta t_i, \mathcal{E} - \Delta\mathcal{E}(\Delta t_i)\big). \tag{S16}$$

This expression is then convoluted with a kernel in two-dimensional energy-shift and time-delay space, in a similar manner to the aforementioned quantum theory, thus reproducing the EELS spectra observed in the experiment.

Comparison of CDEM to other regimes of electron-field interactions

In general, there are three major regimes of interaction that prove to be important when considering free-electron interactions with classical external electromagnetic fields. These regimes are classified according to the duration of the field cycle τ_EM relative to the electron pulse duration and the electron-field interaction duration $\tau_\mathrm{e} \lesssim \tau_\mathrm{int}$ (τ_int appears in the main text as the ratio of the interaction length to the electron velocity, L/v):

[1] $\tau_\mathrm{EM} \ll \tau_\mathrm{e}$: This regime occurs in the extreme case of optical and higher frequency fields (field cycle τ_EM~0.1-10 fs and even below), where the field cycle duration is much shorter than the electron pulse duration (*e.g.*, τ_e~350 fs in our setup). The difference in timescales causes each electron to experience many field cycles. The resulting electron energy spectrum is then similar to photon-induced near-field electron microscopy (PINEM),[45–52] which includes multiple $\hbar\omega$-spaced energy peaks, each of them with a probability corresponding to the emission or absorption of a given number of photon quanta by the electron. Notably, this result can only be accommodated by a quantum mechanical treatment of the free-electron wave function.

[2] $\tau_\mathrm{e}, \tau_\mathrm{int} \ll \tau_\mathrm{EM}$: In the opposite extreme, the field cycle is much longer than both the electron pulse duration and the time taken by that electron to traverse the region of interaction. Consequently, each electron experiences a time-independent field and, hence, undergoes no energy shift (since such fields are conservative). This field can however cause the electron to undergo elastic scattering, changing the electron transverse momentum, as in deflectometry

measurements,[27–29] which can be treated classically. This regime also encompasses electron holography[53] and Lorentz microscopy,[54] where only the electron phase (rather than its amplitude or energy) is altered by the (effectively DC) fields.

[3] Describing all the intermediate regimes requires a general theory as explained above. One such regime is when the field cycle is longer than the electron pulse duration, but shorter than the interaction timescale. This is the regime in which CDEM occurs. For example, consider a field cycle of a few ps (*i.e.*, in the THz region), which is longer than the electron pulse duration, but comparable or shorter than the time it takes the electron to traverse the region of interaction. The electron can be considered as a point particle, but experiences a time-varying field during its interaction (thus, non-conservative fields). Consequently, the overall acceleration and deceleration experienced by the electron does not average to zero, and the resulting electron spectrum can include net gain or loss of energy (*i.e.*, it is strongly asymmetric). This is in contrast to the two other regimes, in which the energy shift averages to zero and the resulting electron energy spectrum is symmetric.

Hydrodynamic model of the photo-Dember effect

This section provides a summary of the hydrodynamic model of the photo-Dember effect observed in our experiment. Simply stated, this model takes us from the pump laser intensity through the spatiotemporal current density distribution inside the InAs crystal and finally to the electric potential outside the crystal.

The mobility difference between photo-excited electrons and holes in InAs, together with the boundary condition imposed by the sample edges, lead to the rapid formation of a macroscopic (micron scale) dipole inside the crystal upon laser excitation. While the lower-mobility holes are bound to the surface, higher-mobility electrons are free to travel under the influence of drift and diffusion. This effect, known as the photo-Dember effect,[42] involves the acceleration of charge carriers on a picosecond timescale and is therefore commonly used as a source of single-cycle THz radiation.

Below we summarize the experimental considerations:

1. We have a p-type InAs bulk sample (dopant concentration of 10^{17} cm^{-3}).
2. An 800 nm, 50 fs FWHM laser pulse with a repetition rate of 1 MHz impinges the sample face along the *x* coordinate – perpendicular to the surface.
3. The laser pulse duration is negligible compared to the other time constants of the system.
4. Immediately after the action of the laser pulse, we have the following density of photo-excited pairs in the semiconductor:
    a. In the normal direction *x*, an exponential profile $n(x) = n_{\mathrm{exc}} e^{-\alpha x}$, where n_{exc} is the number of excited pairs on the surface and $\alpha = 7\ \mu\mathrm{m}^{-1}$ is the absorption coefficient.
    b. In the transverse direction (the *yz* plane), a 2D Gaussian profile that follows the laser spot (40 μm FWHM).
5. Due to the sharp decay of the distribution in the normal direction *x* relative to the much smoother distribution in the transverse direction *yz*, the following approximations can be safely adopted:
    a. The charge dynamics inside the sample can be assumed to be one-dimensional (current density j_x along *x*).
    b. For the purpose of solving the charge dynamics, the geometry can be considered as a semi-infinite sample in the *x* axis, and infinite in the *y* and *z* axes.

The dynamics of the electron-hole distribution in the system can be described using a hydrodynamic model of the photo-Dember effect, as derived by Reklaitis.[44] Using this model, the transient current density inside the sample was shown to be given by:

$$j_x(\boldsymbol{r},t) = en_{\mathrm{exc}} I(\boldsymbol{s}) v_t^2 \alpha e^{-\alpha x} e^{-\frac{\gamma t}{2}} \frac{\sin \omega t}{\omega},$$
$$\omega = \sqrt{\omega_0^2 - \omega_1^2 (1 - e^{-\alpha x})}, \qquad \text{(S17)}$$
$$\omega_0 = \sqrt{\frac{e^2}{\varepsilon}\left(\frac{n_{\mathrm{exc}} I(\boldsymbol{s})}{m^*} + \frac{n_{\mathrm{eq}}}{m_{\mathrm{eq}}}\right) - \frac{\gamma^2}{4}}, \qquad \omega_1 = \sqrt{\frac{e^2}{\varepsilon}\frac{n_{\mathrm{exc}} I(\boldsymbol{s})}{m^*}}.$$

Here, $v_{\mathrm{t}}^2 = v_{\mathrm{te}}^2 - v_{\mathrm{th}}^2 \cong v_{\mathrm{te}}^2$ is the difference between the average squared velocities of electrons and holes immediately after photoexcitation, γ is the momentum relaxation rate associated with collisions inside the sample, n_{eq} is the concentration of equilibrium charges in the semiconductor (in our case, n_{eq} is the doping concentration). m_{eq} is the effective mass of equilibrium charges (here, $m_{\mathrm{eq}} = m_{\mathrm{h}}$), and $m^* = \frac{\tilde{m}_{\mathrm{e}} m_h}{\tilde{m}_{\mathrm{e}} + m_h}$ with $\tilde{m}_{\mathrm{e}}$ and m_{h} denoting the effective masses of electrons and holes, respectively, and the tilde indicates that the electron nonparabolicity has been accounted for (see table S1 below). Also, $I(\boldsymbol{s})$ is the transverse laser-intensity profile (a dimensionless function) in the *yz* plane, while $\boldsymbol{s}$ is a transverse *yz*-plane coordinate, $\boldsymbol{s} = y\hat{y} + z\hat{z}$.
Table S1 summarizes the various parameters that enter our model.

Table S1. Parameters used in the hydrodynamic model of the photo-Dember effect

Parameter symbol	Parameter name	value
α	Absorption coefficient	7 $\mu\mathrm{m}^{-1}$
ε	Dielectric permittivity	$12.3\varepsilon_0$
γ	Momentum relaxation rate	$3.3 \cdot 10^{12}\ \mathrm{s}^{-1}$
m_h	Hole effective mass	$0.6m_0$
m_{e}	Electron effective mass (low energy)	$0.022m_0$
$\lambda, h\upsilon$	Excitation laser wavelength and energy	800 nm, 1.55 eV
E_g	Band gap energy	0.354 eV
α_Γ	Conduction band nonparabolicity	2.2 eV^{-1}
n_{eq}	Density of equilibrium carriers (holes)	$10^{17}\ \mathrm{cm}^{-3}$
v_{te}^2	Electron average squared velocity	$\frac{2\varepsilon_e}{3m_e}\frac{1+\alpha_\Gamma\varepsilon_e}{1+4\alpha_\Gamma\varepsilon_e(1+\alpha_\Gamma\varepsilon_e)} = \left(7.661 \cdot 10^5\ \frac{\mathrm{m}}{\mathrm{s}}\right)^2$
ε_e	Energy of photoexcited electrons	$\frac{2(h\upsilon - E_g)m_h}{m_e + m_h + \left[(m_e+m_h)^2 + 4\alpha_\Gamma(h\upsilon - E_g)m_e m_h\right]^{1/2}} = 1.065$ eV
$\tilde{m}_{\mathrm{e}}$	Photoelectron effective mass	$m_e\frac{3[1+4\alpha_\Gamma\varepsilon_e(1+\alpha_\Gamma\varepsilon_e)]^{3/2}}{3+8\alpha_\Gamma\varepsilon_e(1+\alpha_\Gamma\varepsilon_e)} = 0.185m_0$

We now evaluate the resulting potential, and note that only E_z can change the electron energy (due to the paraxial approximation, as discussed in the CDEM theory above).

Adopting the Lorenz gauge, the following formulae can be used to find the potentials:

$$\begin{aligned}\boldsymbol{A}(\boldsymbol{r},t) &= \frac{\mu_0}{4\pi}\int \frac{\boldsymbol{j}(\boldsymbol{r}',t_r)}{|\boldsymbol{r}-\boldsymbol{r}'|}d^3\boldsymbol{r}',\\ \Phi(\boldsymbol{r},t) &= \frac{1}{4\pi\varepsilon_0}\int \frac{\rho(\boldsymbol{r}',t_r)}{|\boldsymbol{r}-\boldsymbol{r}'|}d^3\boldsymbol{r}',\end{aligned} \tag{S18}$$

where we use the retarded time defined by

$$t_r = t - \frac{\sqrt{(x-x')^2+(y-y')^2+(z-z')^2}}{c}. \tag{S19}$$

According to these expressions, we have $A_z = 0$ since $j_z = 0$, and thus,

$$E_z = -\frac{\partial\Phi}{\partial z} - \frac{\partial A_z}{\partial t} = -\frac{\partial\Phi}{\partial z}. \tag{S20}$$

Let us now find the charge density ρ. Neglecting band bending near the crystal edges, before the interaction we have a constant and uniform charge density $\rho_0 = en_{\mathrm{eq}}$ across the crystal. To find the charge density after the interaction, we invoke the continuity equation

$$\frac{\partial\rho(\boldsymbol{r},t)}{\partial t} + \frac{\partial j_x(\boldsymbol{r},t)}{\partial x} = 0, \tag{S21}$$

and hence,

$$\rho(\boldsymbol{r},t) = \rho_0 - \int_0^t \frac{\partial j_x(\boldsymbol{r},\tau)}{\partial x}d\tau. \tag{S22}$$

We can neglect the constant part ρ_0 because it does not create any energy gain or loss. Also, we should consider the boundary condition $j_x(x<0,y,z,t)=0$. Therefore, we have a surface charge density σ on the boundary given by

$$\sigma(y,z,t) = -\int_0^t j_x(x=0,y,z,\tau)\,d\tau. \tag{S23}$$

Now, we can find the scalar potential:

$$\Phi(\mathbf{r},\mathrm{t}) = \frac{1}{4\pi\varepsilon_0}\left(\int \frac{-\int_0^t \frac{\partial j_x(\boldsymbol{r}',\tau)}{\partial x'}d\tau}{|\boldsymbol{r}-\boldsymbol{r}'|}d^3\boldsymbol{r}' + \int \frac{-\int_0^t j_x(x'=0,y',z',\tau)}{|\boldsymbol{r}-\boldsymbol{s}'|}d\boldsymbol{s}'\right), \tag{S24}$$

$$\Phi(\boldsymbol{r},t) = \frac{-1}{4\pi\varepsilon_0}\left(\int \frac{\int_0^t \frac{\partial j_x(\boldsymbol{r}',\tau)}{\partial x'}d\tau\,dx'dy'dz'}{\sqrt{(x-x')^2+(y-y')^2+(z-z')^2}} + \int \frac{\int_0^t j_x(x'=0,y',z',\tau)\,dy'dz'}{\sqrt{(x-0)^2+(y-y')^2+(z-z')^2}}\right).$$

Integrating by parts, we obtain

$$\Phi(\boldsymbol{r},t) = \frac{1}{4\pi\varepsilon_0}\left(\int dy'dz'\int_0^{+\infty} dx' \frac{\int_0^t j_x(\boldsymbol{r}',\tau)\,d\tau\cdot(x'-x)}{((x-x')^2+(y-y')^2+(z-z')^2)^{3/2}}\right), \tag{S25}$$

where j_x is taken from the hydrodynamic model of the photo-Dember effect (Eq. (S17)):

$$\int_0^t j_x(\boldsymbol{r}',\tau)\,d\tau = -\frac{en_{\mathrm{exc}}I(\boldsymbol{s})v_t^2\alpha e^{-\alpha x'}}{\omega(\gamma^2+4\omega^2)}(4\omega\cos\omega t + 2\gamma\sin\omega t)e^{-\frac{\gamma t}{2}}. \tag{S26}$$

Through Eqs. (S4) and (S7), the calculated scalar potential is then used to evaluate the evolution of the electron wave function following the interaction with the field, and finally obtain the resulting electron spectrum.

Complete model for the electron-field interaction, also considering the triangular sample geometry

This section describes how we use the CDEM theory as part of an end-to-end model of the electron-field interaction, considering the triangular sample geometry used in the experiment. We rely on the hydrodynamic model from the previous section, which provides the dynamics of the charge density $\rho(\boldsymbol{r},t)$ inside the crystal. This density can be evaluated using a semi-infinite sample geometry, despite the non-trivial boundary conditions imposed by the triangular shape of the actual specimen, because the charge dynamics is confined near the area of laser excitation.

In a semi-infinite sample (ROI 2 in Figure S1), we employ a fully analytical approach, as described in the previous section. If, however, one wishes to analyze the results shown in Figure 2 of the main text, the full sample geometry must be considered. We go beyond the charge distribution and analyze the created THz field and the electron-field interaction, which depend on the bulk charge distribution in a way that is sensitive to the boundary conditions.

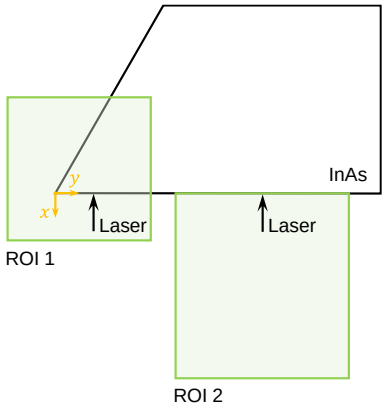

Figure S1. The different sample geometries considered in our experiment. We show a lateral plane (*xy*) illustration of such sample geometries. The green rectangles mark the two regions of interest (ROIs), along with the respective position of the incident pump laser (black arrow). Each ROI defines a region in the *xy* plane for which we calculate the field given a certain laser excitation. ROI 1 matches Figure 2 of the main text, while ROI 2 matches Figure S2.

In the data shown in Figures 2A and 2B, there is some illumination of the triangular corner region. Unfortunately, considering the contribution of charge-carrier accumulation at the tip is a rather complicated task and was therefore left aside for the current work. Of course, in the simulations shown in Figures 2B and 3, the charge carriers and THz field dynamics were simulated taking the triangular sample boundary conditions into account.

To model the THz pulse propagation in a triangular sample (ROI 1 in Figure S1), as is the case in Figure 2 of the main text, we employ a numerical approach. For this purpose, we use the Electrostatics module provided in COMSOL Multiphysics, which solves the Poisson equation both inside and outside the sample, incorporating the bulk $\rho(\boldsymbol{r},t)$ and surface $\sigma(y,z,t)$ charge densities, as well as the current density $j_x(\boldsymbol{r},t)$, given in the previous section (Eqs. (S15), (S20), and (S21)).

The charge distribution $\rho(\boldsymbol{r},t)$ is shown in the insets of Figures 2B and 3 of the main text. The reconstruction of the ultrafast charge dynamics is done by fitting this theory to the experimental

data. The theory-experiment fit applied in the reconstruction compares the entire electron spectrum collected at each *xy* point. However, since the experimental information is five-dimensional, Figure 2 of the main text presents only the mean electron energy shifts (for a pump pulse energy of 10 nJ).

The reconstruction of the charge dynamics can be improved by several orders of magnitude in different dimensions. For example, shorter electron pulse durations (currently ~350 fs) could provide higher time resolution. Similarly, using narrower electron energy width (currently ~1.1 eV) could improve the sensitivity of CDEM to enable capturing features associated with lower charge densities. Working with a smaller electron probe (currently 1 μm) would improve the spatial resolution, only limited by the microscope magnification that can reach sub-nanometer spot sizes. CDEM with higher spatial resolution can be accomplished already with the existing setup at the expense of a reduced field of view.

General principles for the sensitivity of CDEM: guidelines for applications in other systems

In this section, we provide estimates for the feasibility of the CDEM approach beyond the current work, namely, what other effects can be observed *via* CDEM, and what is the expected sensitivity. We consider a time-harmonic line current density element $j_x(\boldsymbol{r},t)$ situated in the lateral *xy* plane:

$$j_x = I_0\big(\theta(\mathrm{x}) - \theta(\mathrm{x}-\mathrm{d})\big)\,\delta(y)\delta(z)\cos\omega t\,. \tag{S27}$$

The probe-electron passes along the *z* axis, near this element or through it, interacting with the emitted near field and undergoing an energy shift as a result. To analyze the sensitivity of the CDEM technique, we need to find the minimum current density values for which the map of electron energy shifts has a sufficiently large contrast to provide a signal (this depends on the resolution of the electron (energy) spectrometer and the electron energy width). We note that the mentioned current element can be regarded as a prototypical building block for arbitrarily more complex charge distributions (in particular, an arbitrary current density could be synthesized by superposing these line sources), and hence, the setup considered here, beyond being reasonably representative, is also readily extendable to more complex current distributions.

The scalar potential created by the current density, according to Eq. (S24), is given by

$$\Phi(\mathbf{r},\mathrm{t}) = \frac{1}{4\pi\varepsilon_0}\int \frac{-\int_0^t \frac{\partial j_x(\boldsymbol{r}',\tau)}{\partial x'}\,d\tau}{|\boldsymbol{r}-\boldsymbol{r}'|}\,d^3\boldsymbol{r}'\,. \tag{S28}$$

Pluging Eq. (S27) in, we obtain

$$\int_0^t \frac{\partial j_x(\boldsymbol{r}',\tau)}{\partial x'}\,d\tau = I_0\big(\delta(x') - \delta(x'-\mathrm{d})\big)\,\delta(y')\delta(z')\,\frac{\sin\omega t}{\omega}, \tag{S29}$$

$$\begin{aligned}\Phi(\mathbf{r},\mathrm{t}) &= \frac{I_0}{4\pi\varepsilon_0}\frac{\sin\omega t}{\omega}\int \frac{-\big(\delta(x') - \delta(x'-\mathrm{d})\big)\,\delta(y')\delta(z')}{((x-x')^2+(y-y')^2+(z-z')^2)^{1/2}}\,d^3\boldsymbol{r}' \\ &= -\frac{I_0}{4\pi\varepsilon_0}\frac{\sin\omega t}{\omega}\left(\frac{1}{(x^2+\mathrm{y}^2+\mathrm{z}^2)^{1/2}} - \frac{1}{((x-d)^2+\mathrm{y}^2+\mathrm{z}^2)^{1/2}}\right).\end{aligned} \tag{S30}$$

The electric field according to Eq. (S20) reads

$$E_z = \frac{3I_0}{4\pi\varepsilon_0}\frac{\sin\omega t}{\omega}\,z\left(\frac{1}{(x^2+\mathrm{y}^2+\mathrm{z}^2)^{3/2}} - \frac{1}{((x-d)^2+\mathrm{y}^2+\mathrm{z}^2)^{3/2}}\right). \tag{S31}$$

We can assume that the electron trajectory is a straight line along z such that $z = v\cdot(t-\Delta t)$, where Δt is the time delay. Without loss of generality, we assume that the electron trajectory crosses the $z=0$ plane at $x=-x_0,\ y=0$.

The energy shift of the electron can be quantified as

$$\Delta\mathcal{E}(\Delta t) = mc^2\Delta\gamma = \frac{p_z}{m\gamma}\,\Delta p_z = ev\int_{-\infty}^{+\infty} E_z(-x_0, 0, z(t,\Delta t), t)dt\,, \tag{S32}$$

with the integral taken along the electron trajectory.
Pluging the electric field (Eq. (S31)) in Eq. (S32), and evaluating the integral, we finally obtain

$$\Delta\mathcal{E}(\Delta t) = \frac{3eI_0}{2\pi\varepsilon_0 v}\cos\omega\Delta t\left(K_0\left(\frac{\omega x_0}{v}\right) - K_0\left(\frac{\omega(x_0+d)}{v}\right)\right), \tag{S33}$$

where K_0 is the zeroth order modified Bessel function of the second kind. The largest energy shift is found for a time delay $\Delta t = 0$. Furthermore, for the relevant THz frequencies, the dimensionless part of Eq. (S33) is of the order of unity:

$$K_0\left(\frac{\omega x_0}{v}\right) - K_0\left(\frac{\omega(x_0+d)}{v}\right) \approx 2.4,$$

calculated for $\omega = 10^{12}$ Hz, $x_0 = 100$ nm, $d = 1\ \mu$m, and $v = 10^8$ m/s. Thus, we can estimate the magnitude of the effect as

$$\Delta\mathcal{E} \sim \frac{3eI_0}{2\pi\varepsilon_0 v}. \tag{S34}$$

Let us argue why Eq. (S34) provides a correct estimate for the photo-Dember effect discussed in the main text. From the charge density reconstruction, we have the minimum observable current density $j \cong 10^8$ A/m^2, obtained for a pump laser pulse energy of 0.05 nJ and a laser spot area of about 10^{-10} m^2, resulting in a total current of $I_0 \cong 10^{-2}$ A. According to Eq. (S34), such a current gives a maximal energy shift of the order of 0.1eV, which is in good correspondence with the experimental results.
Consequently, we can now consider other systems for which the ultrafast nanoscale charge dynamics is of interest. We can use Eq. (S34) to estimate the relevance of CDEM for any system with charge dynamics possessing nanometer-picosecond spatiotemporal features. The most critical parameter for estimating the relevance of CDEM is the effective current I_0 that describes the charge dynamics. On the microscopic level, I_0 can be related to the number of charge carriers participating in the process. If we consider the motion of a single electron, with changes on the 1 ps timescale, the relevant current is $I_0 = 1.6\cdot 10^{-7}$ A. Substituting in Eq. (S34), this results in an energy shift of $1.4\cdot 10^{-5}$ eV (for an electron probe with a kinetic energy of 200 keV as in our experiment). Consequently, an electron spectrometer with such energy resolution would make it possible for CDEM to probe the dynamics of a single electron. Any phenomenon of charge dynamics that involves a larger number of electrons would increase the signal in proportion to the number of electrons. In the current work, the signal is created by the motion of ~10^4-10^5 charge carriers. State-of-the-art electron spectrometers reach an energy resolution near 1 meV[43] and could thus reduce the required number of charge carriers to 10^2. Observing Eq. (S34), we note that using slower probe electrons would also increase the sensitivity of CDEM.

We now estimate the expected energy shift for a particular example: a superconductor phase transition. Consider a vortex tube of a single magnetic flux quantum ($\Phi_0 = h/2e$) trapped in a type-II superconductor. The magnetic field distribution of a single vortex in the $r \to 0$ limit is given by[59]

$$B(r\to 0) \cong \frac{\Phi_0}{2\pi\,\lambda^2}\ln\kappa\,, \tag{S35}$$

where $\kappa = \lambda/\xi$ is the Ginzburg-Landau parameter, ξ is the superconducting coherence length (from Ginzburg-Landau theory), and λ is the London penetration depth. From magnetostatics, the magnetic field at the vortex center is connected to the total current in the loop circumference via

$$B(r = 0) = \frac{\mu_0}{2R} I, \tag{S36}$$

where $R = \xi$ is the vortex radius. Equating both expressions for the magnetic field, we retrieve the total current:

$$I = \frac{\hbar}{e\mu_0} \frac{\ln \kappa}{\lambda \kappa}. \tag{S37}$$

Since $\kappa > 1/\sqrt{2}$ in type-II superconductors, using a conservative estimate for the London penetration depth ($\lambda = 100$ nm), we obtain a typical current of 10^{-3} A. The ability of CDEM to detect such a vortex loop being created or annihilated, on the characteristic 1-10 ps timescale,[57] depends on both the coherence length and the London penetration depth of the superconducting material. According to Eq. (S34), the expected energy shift is of the order of 10 meV, which is right on the frontier of current electron spectrometers in state-of-the-art TEMs. This value can be increased by using a superconducting material with a longer coherence length or shorter London penetration depth.

References

78. Friedman, A.; Gover, A.; Kunzki, G.; Ruschin, S.; Yariv, A. Spontaneous and Stimulated Emission from Quasifree Electrons. *Rev. Mod. Phys.* **1988**, *60*, 471–535.

Spatiotemporal maps of electron energy shifts for a straight-edge sample geometry

This section presents additional CDEM experiments performed on a sample with a different geometry. Figure S2 provides a clearer view of the THz pulse free-space propagation, repeating the STEM-EELS measurements shown in Figure 2A of the main text for a simpler straight-edge crystal geometry (*i.e.*, without a triangular tip, as depicted in Figure S1). Moreover, the results in Figure S2 are captured using a larger field of view relative to Figure 2A ($140 \times 150\ \mu m^2$), obtained by tuning the electron lens current. In this way, certain features of the THz pulse near-field evolution are better elucidated.

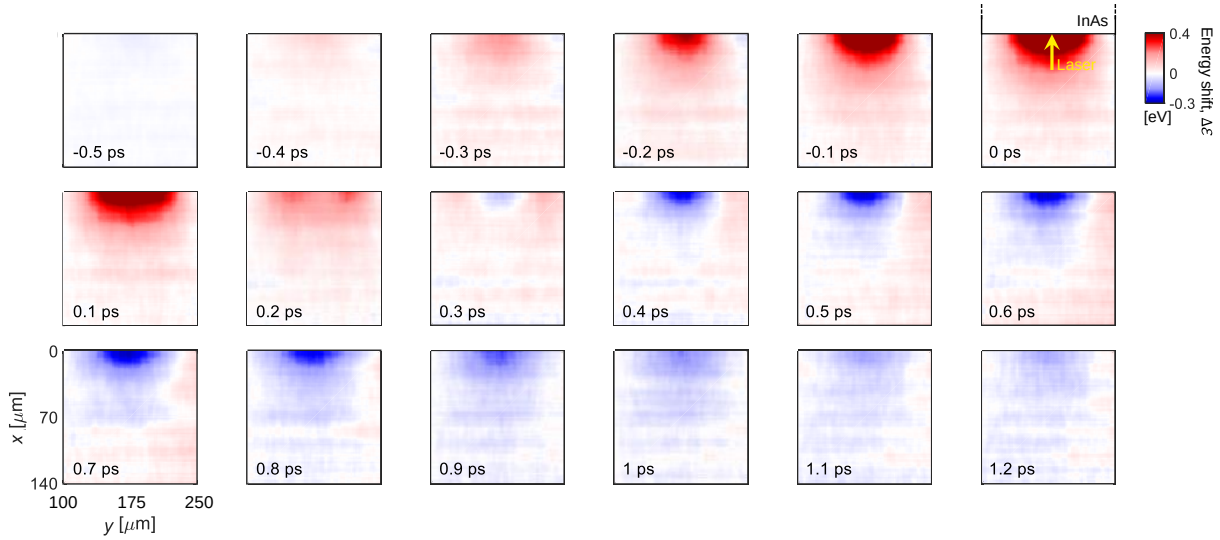

Figure S2. Spatiotemporal maps of electron energy shifts for a straight-edge sample geometry. These maps of electron energy shifts are captured in a similar fashion to the ones displayed in Figure 2A of the main text, but for a straight-edge crystal (*i.e.*, without a triangular tip) and setting the electron lenses to obtain a larger field of view. The pump laser pulse is traveling along the x axis, impinging the crystal normal to the surface at the $x = 0$ plane (yellow arrow in the 0 ps panel). The pump pulse energy is 10 nJ.

Spatiotemporal maps of electron energy shifts focusing on the InAs crystal tip

This section presents additional CDEM experiments, focusing on a smaller $5 \times 5\ \mu m^2$ region around the InAs crystal tip. Parts of this data are also shown in Figure 2C of the main text.

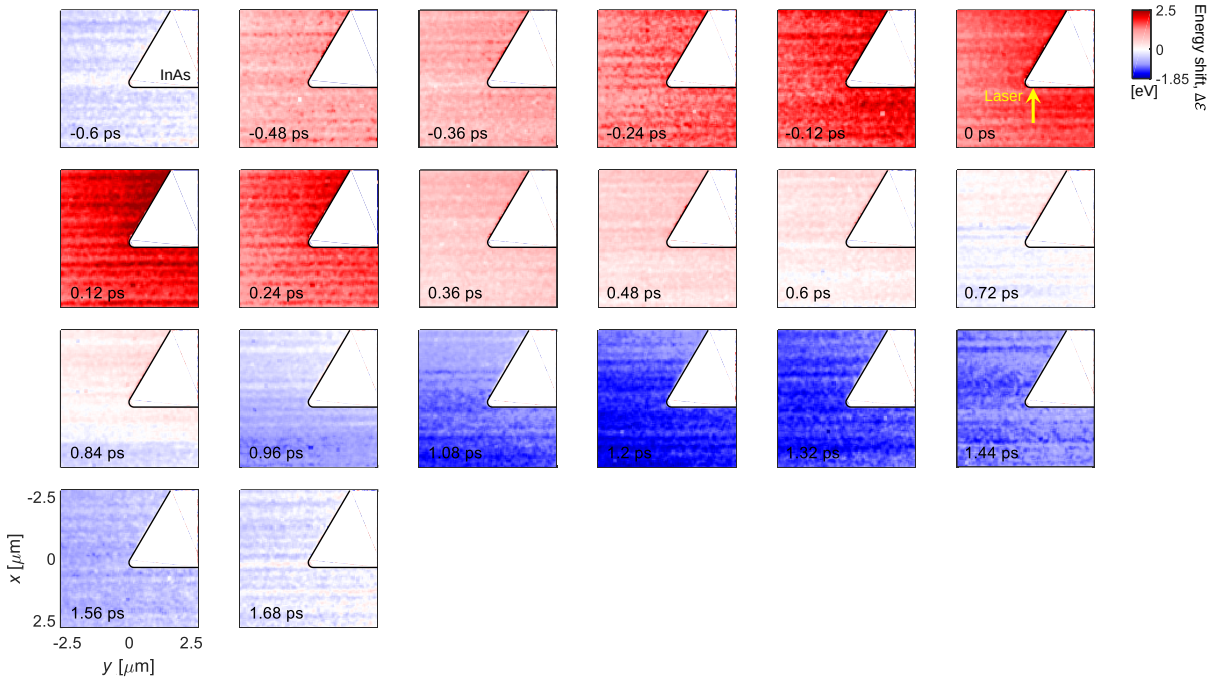

Figure S3. Spatiotemporal maps of electron energy shifts focusing on the InAs crystal tip. Measured spatiotemporal maps of electron-beam energy shifts, focusing on the InAs crystal tip ($5 \times 5\ \mu m^2$ region), with probe electron spot size of 50 nm. The pump laser pulse is incident along the *x* axis, normal to the crystal surface and centered at the tip ($x,y,z = 0$), as illustrated by the yellow arrow in the 0 ps panel.

Movie S1. Spatiotemporal maps of electron energy shifts for the triangular geometry. Movie of the data presented in the panels of Figure 2A of the main text.

Movie S2. Spatiotemporal maps of electron energy shifts for the straight-edge geometry. Movie of the data presented in the panels of Figure S2.

Movie S3. Spatiotemporal evolution of the reconstructed charge density. Movie depicting a three-dimensional reconstruction of the charge density, in which the InAs crystal is cut along the $z = 0$ and $x = 0$ planes.